CrossMark

ORIGINAL ARTICLE

Anisotropic masonry failure criterion using artificial neural networks

Panagiotis G. Asteris[1] · Vagelis Plevris[1]

Abstract In the last decades, a plethora of advanced computational models and techniques have been proposed on the modeling, assessment and design of masonry structures. The successful application of such sophisticated models necessitates the development of reliable analytical models capable of describing the failure of masonry materials. Nevertheless, there is a lack of analytical models due to the anisotropic and brittle nature exhibited by the masonry materials. In the present paper, the use of neural networks (NNs) is proposed to approximate the failure surface of masonry materials in dimensionless form. The comparison of the derived results with experimental findings as well as analytical results demonstrates the promising potential of using NNs for the reliable and robust approximation of the masonry failure surface under biaxial stress.

1 Introduction

Masonry exhibits distinct directional properties due to the influence of the mortar joints. Depending upon the orientation of the joints to the stress directions, failure can occur in the joints alone or simultaneously in the joints and the blocks. Nowadays, in developed societies, there is an increased interest about reliable and robust computational models for the modeling of masonry structures. This is primarily due to the growing interest of protecting heritage structures. The main characteristic of the majority of these structures is that they are mostly made of masonry materials.

To fulfill this need, in the last decades a large number of macro and micro computational models have been proposed both for linear and nonlinear analysis of such structures [1–6]. Detailed and in-depth state-of-the-art reports can be found in Lourenço [7], Roca et al. [8], Asteris et al. [9, 10], Sarhosis [11] and Plevris and Asteris [12].

The successful implementation of these advanced models requires reliable analytical constitutive rules such as constitutive equation models of masonry material failure, which is not the case at the present. To date, research work has been focused on isotropic masonry models, which are based, primarily, on models applied for concrete [13]. Regarding non-isotropic masonry, there are a few research works in which failure criteria approximate the failure surface by employing different forms of quadratic polynomials. Many variations of such models have been published to date, including those that define the failure surface through the use of different functions for each quadrant [14–19]. However, for certain load cases, such models overestimate strength [20].

The main disadvantage of the above criteria is that the corresponding failure surface is a synthesis of at least four individual surfaces (one for each quadrant). This leads to the formation of singular points, namely "corners" (curves at which the individual surfaces intersect) where the flow vector is not uniquely defined [21, 22], thus leading to

✉ Panagiotis G. Asteris
 panagiotisasteris@gmail.com

 Vagelis Plevris
 vplevris@gmail.com

[1] Computational Mechanics Laboratory, Department of Civil Engineering, School of Pedagogical and Technological Education (ASPETE), 141 21 Heraklion, Athens, Greece

indeterminate direction of straining. The existence of singular points causes significant problems to nonlinear analysis [23]. In order to avoid the formation of such points, the use of a closed continuous yield surface described analytically by a single function (cubic polynomial) has been recently proposed [24–26].

During the last decades, neural networks have been used extensively for various applications in civil engineering [27–30] and earthquake engineering [31, 32], including many attempts on modeling the materials' constitutive rules [33–38]; however, to the authors' knowledge, there have not been many attempts to apply a neural network (NN) for the prediction of masonry behavior in general. The only proposal in this area is that of a previous work by the authors [12] in which a novel method has been proposed by applying neural networks (NNs) to approximate the masonry failure surface [limited only for the case of biaxial compressive (only) stress state]. The method comprises a series of NNs that are trained with available experimental data. The results demonstrate the great potential of using NNs for the approximation of masonry failure surface under biaxial compressive stress.

In the present paper, following the work undertaken above, the use of neural networks is proposed for modeling the anisotropic masonry behavior under biaxial stress state. In particular, a novel procedure based on NN techniques has been introduced for acquiring the failure/yield surface of masonry material in a dimensionless form, taking into account available experimental results from the literature as input data for the training and validation of NNs. It is the first time this has been achieved in a dimensionless form, for any quadrant of the masonry stress state.

2 Methodology

The highly anisotropic brittle nature of masonry renders complicated, difficult and expensive the realization of reliable experimental tests under conditions of biaxial stress, and, even more, under conditions of biaxial tension or heterogeneous stress. The angle of the applied loading to the bed joint plays a significant role in the behavior of the brick masonry disks. In general, the highest strength of masonry is observed when the compressive load is perpendicular to the bed joints or in other words when the principal tensile stress at the center of the disk is parallel to the bed joints. In this case, failure occurs through bricks and perpendicular joints. On the other hand, the lowest strength is observed when the compressive load is parallel to the bed joints or in other words when the principal tensile stress at the center of the disk is perpendicular to the bed joints. In this case, failure occurs along the interface of brick and mortar joint.

The methodology of the present work is similar to another study by the authors [12]. That previous work focused only on the compression–compression area, where both principal stresses were compressive, i.e. it focused on the third quadrant of the σ_I–σ_{II} plane (compression–compression), without having to do with the other three quadrants. The present work extends the investigation to all four quadrants, namely the (A) tension–tension, (B) compression–tension, (C) compression–compression and (D) tension–compression quadrant. The former work utilized the experimental data reported by Page [39–41], which have been already used by many other researchers [26, 42, 43]. Ratios of vertical compressive stress σ_I to horizontal compressive stress σ_{II} of 1, 2, 4, 10 and ∞ (uniaxial σ_I) have been used in conjunction with a bed joint angle θ with respect to σ_I, in directions of 0°, 22.5°, 45°, 67.5° and 90°. A minimum of four tests were performed for each combination of σ_I/σ_{II} and θ.

The present study applies neural networks in order to approximate the experimental failure curves of a brittle anisotropic material such as masonry. The aim of the study was to introduce an anisotropic (orthotropic) neural network—generated 3D failure surface under biaxial stress for masonry for any angle of the joints to the vertical compressive load, as described in detail in the next paragraphs. First, for each angle θ (0°, 22.5°, 45°, 67.5°, 90°) of the joints to the vertical compressive load, a neural network was trained with the experimental data of Page [39–41] as inputs (5 NNs in total). Then each one of the five NNs was asked to produce the whole 2D failure curve for each angle θ as its output, filling also the gaps between the experimental points, thus "enriching" the experimental data with appropriate approximations. Then another, bigger, "global" NN was trained using the results of the five NNs as inputs with the angle θ as an input, also. The new NN was then asked to fill also the gaps between the angles θ, providing the whole 3D failure surface (a tube) for any angle θ (0°–90°) and any ratio of σ_I/σ_{II}, for all four quadrants of stress.

3 Biaxial testing procedure

Masonry is a composite, multi-phase material that depicts distinct brittle and strongly anisotropic nature, making complicated, difficult and expensive, the realization of reliable experimental tests under conditions of biaxial stress, and, even more, under conditions of biaxial tension or heterogeneous stress. In the next sections, the process of both the preparation of test specimens and the tests conducted under biaxial stress state are presented in detail, with special attention to the parameters that affect the results. At this point, it should be emphasized that available

experimental results obtained by other researchers are used in this paper.

3.1 Preparation of test specimens

Two main methodologies are used in the literature in order to obtain the final test specimens with the correct shape and size, presented in Samarasinghe [44], Page [39–41] and Tasios and Vachliotis [45].

3.1.1 The first methodology

Specimens with horizontal and vertical joints (Fig. 1a) are constructed with dimensions greater than those of the final specimen, and then a square with the desired dimensions is drawn on the surface of the wall by a pencil at the appropriate orientation to achieve the correct layup angle as shown in Fig. 1b.

Angle θ denotes the bed joint angle with respect to the horizontal direction, as shown in the figure, which can be also defined as the angle between the direction of the bed joints and one of the edges of the finished test specimen. After a time-span of 14 days, the larger wall panels were cut to the required size and shape by a "Clipper" saw (Fig. 1b) which has the capacity to hold impregnated diamond edge circular blades of varying thickness and diameters. Two days prior to the date of testing, the "compressive edge" of the panel (the side on which the compressive load was to be applied) was capped with 1:1 (cement/sand) mortar [12].

3.1.2 The second methodology

According to Page [39–41], all specimens are constructed directly to their final shape and size as follows: All brickwork is constructed horizontally on a rigid form with bricks glued to a Perspex backing sheet to ensure a constant joint thickness. Panels are made with varying bed joint angles by cutting individual bricks to the required shape before casting.

In the present study, five layup angles were selected for biaxial tests, namely 0°, 22.5°, 45°, 67.5° and 90°.

3.2 Testing rig

A biaxial stress state is induced in the panel by loading with hydraulic jacks in two orthogonal directions, as shown in Fig. 2. A constant load ratio is maintained during each test by means of the spreader beam. The load in each direction is monitored by load cells immediately adjacent to the specimen.

4 Biaxial compression tests

For all panels that were tested by Page [39–41], ratios of compressive stress σ_I to horizontal compressive stress σ_{II} of 1, 2, 4, 10 and infinity (i.e. uniaxial σ_I) were used in conjunction with bed joint angle θ with respect to the σ_I direction of 0°, 22.5°, 45°, 67.5° and 90°. Figure 3 shows the saw-cut specimens and stress directions for the five cases $\theta = 0.0°$, $\theta = 22.5°$, $\theta = 45.0°$, $\theta = 67.5°$ and $\theta = 90.0°$. The cases a(0°)–e(90°), b(22.5°)–d(67.5°) are symmetric to each other, that is why they have been put one under the other in the figure. Principal stress ratios of 0 (i.e. uniaxial σ_{II}), 0.1, 0.25, 0.5 and 1 were obtained from the results using the symmetry of the panels and the loading. A minimum of four tests were performed for each combination of σ_I/σ_{II} and θ. The failure envelopes that Page obtained by plotting mean curves for each bed joint angle can be found in Page [39–41] and Plevris and Asteris [12]. These failure envelopes are based on the peak strength values obtained from running bond masonry panel tests in which a uniform loading was applied proportionally.

It should be noted that there are no real experimental data for the cases (d) $\theta = 67.5°$ and (e) $\theta = 90.0°$, because

Fig. 1 Preparation of the masonry specimens. **a** Wall panel before saw cut, **b** saw-cut specimen

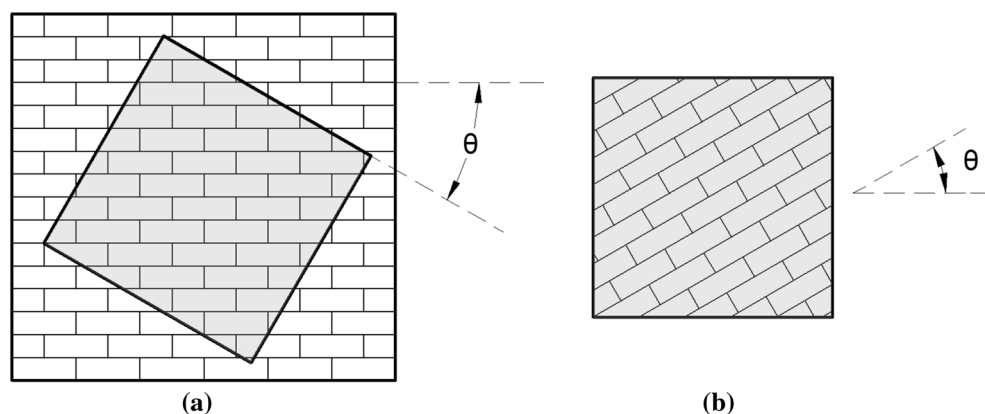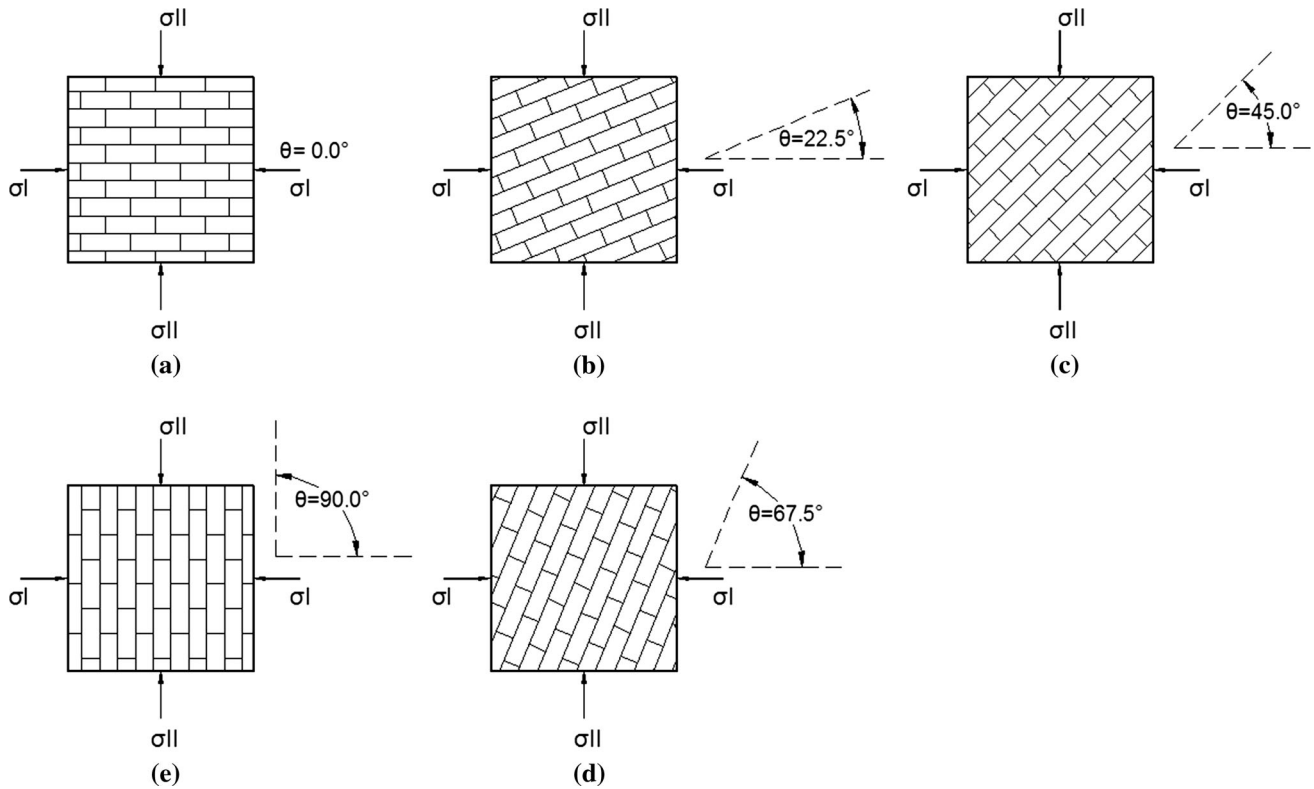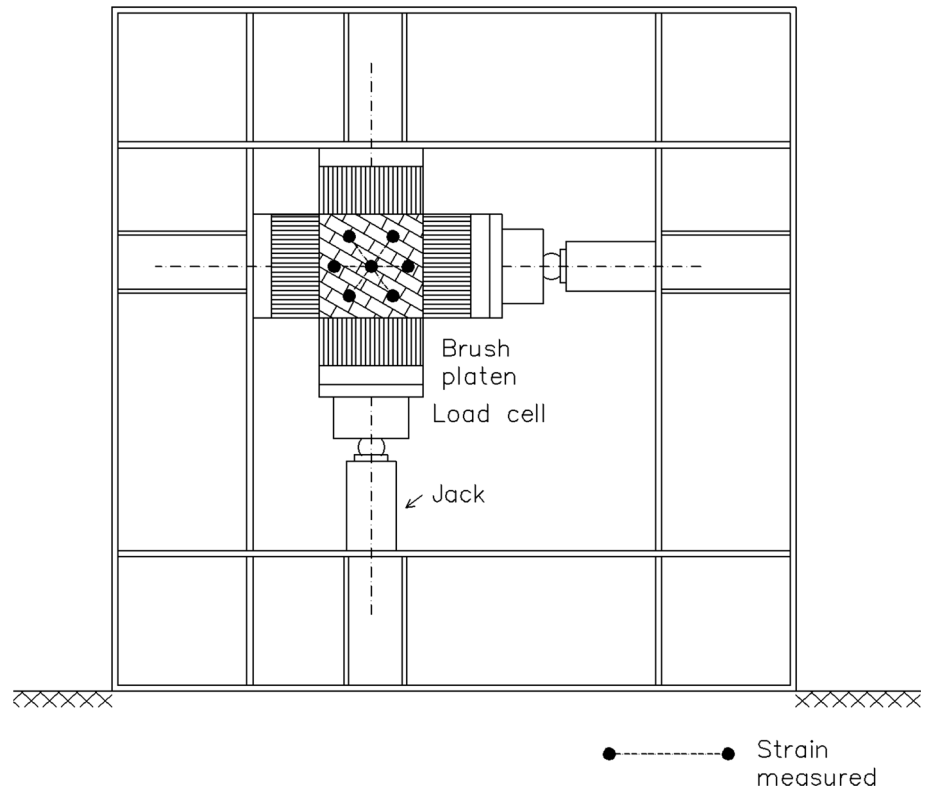(a)   (b)

Fig. 2 Biaxial testing rig

Fig. 3 Saw-cut specimens and stress directions. **a** $\theta = 0.0°$, **b** $\theta = 22.5°$, **c** $\theta = 45.0°$, **d** $\theta = 67.5°$, **e** $\theta = 90.0°$ [39–41]

these cases are equivalent to the cases (b) $\theta = 22.5°$ and (a) $\theta = 0.0°$, respectively, if we reverse σ_I and σ_{II}, as shown in Fig. 3.

5 Artificial neural networks

In the present study, we use *Back-Propagation Neural Networks* (BPNNs), in which the output values are compared with the correct answer to compute the value of a predefined error function. The error is then fed back through the network. Using this information, the algorithm adjusts the weights of each connection in order to reduce the value of the error function by some small amount. The procedure is similar to the one used in a previous work by the authors [12], where more details can be found. The transfer function used in the present study is the hyperbolic tangent function, the same for all the hidden and the input layer, which yields output values in the interval $[-1, 1]$, while its derivative yields output values in the interval $[0, 1]$. The transfer function for the output layer is a linear function. This scheme has been used in all the NNs of the study.

6 Five NN models (for each angle θ)

6.1 NN architecture

For all five NNs, we used a BPNN with one hidden layer, one input layer and one output layer. The input layer had one node (neuron) which corresponds to the angle φ (in the range $[0, 2\pi]$), which defines the ratio σ_{II}/σ_I, while the output layer had also one node which corresponds to the distance (radius) r of the point on the failure curve to the origin of the axes. These two important parameters (φ and r) will be described in detail in the next paragraphs. The hidden layer of each NN had 4 nodes for all θ ($\theta = 0°$, 22.5°, 45°, 67.5°, 90°), ending in a 1-4-1 BPNN architecture for all five cases. These values have been chosen after some trial tests on various network architectures. The input and output values are normalized before the NN training and the inverse normalization is performed in order to take the NN results for other data afterward. It should be noted that the very same NN architecture was used for all five cases with no exceptions.

6.2 Preparation of the NN input data

The experimental data of Page [39–41] have been used as inputs for the first five NN models of the present study. The figure below shows the original data for the $\theta = 0°$ case (in a normalized form, shown as blue points in the figure)
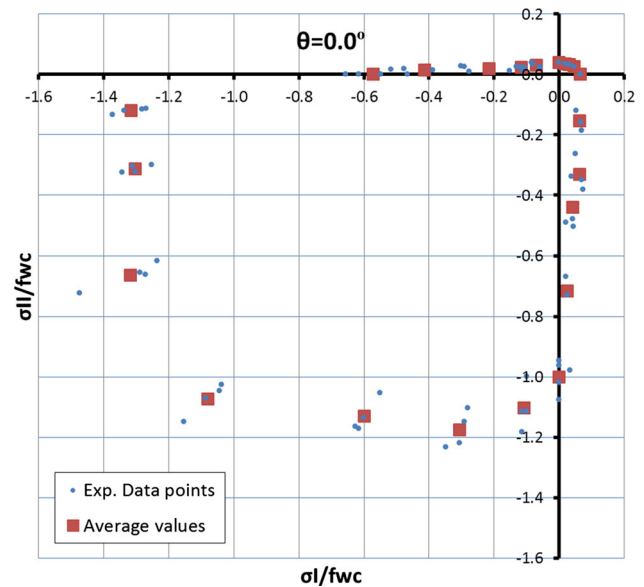

Fig. 4 Normalized experimental data and average values for the $\theta = 0.0°$ case

together with the average values for each σ_I/σ_{II} ratio (shown as red squares) (Fig. 4).

Table 2 (in the "Appendix") shows the corresponding analytical data for the $\theta = 0°$ case. The table consists of four parts, which correspond to four different types of test, published in three different papers, as shown below:

(A) 1st quadrant: biaxial tension ($\sigma_I \geq 0$, $\sigma_{II} \geq 0$), Page [39]
(B) 2nd quadrant: biaxial heterossemous stresses (compression–tension) ($\sigma_I \leq 0$, $\sigma_{II} \geq 0$), Page [41]
(C) 3rd quadrant: biaxial compression ($\sigma_I \leq 0$, $\sigma_{II} \leq 0$), Page [40]
(D) 4th quadrant: biaxial heterossemous stresses (tension–compression) ($\sigma_I \geq 0$, $\sigma_{II} \leq 0$), Page [41]

The first two columns of the table contain the original experimental data, namely the failure principal stresses σ_I and σ_{II} in MPa. The next two columns (columns 3, 4) contain the same data in a dimensionless form where the stresses have been divided with the stress f_{wc} which is the masonry strength for the case $\sigma_I = 0$ for Case C (compression–compression case). The value of f_{wc} has been calculated as the average of the four values (highlighted in bold in the above table) as 7.56 MPa.

In Parts B, C, D we have 2, 3 or 4 tests for every σ_I/σ_{II} ratio. The tension–tension experimental test is the most difficult to perform and also the values are small and the data points more dense, so there is only one test for every σ_I/σ_{II} ratio. The next two columns (columns 5, 6) are the averages of the tests for each loading case, i.e. for each σ_{II}/σ_I ratio. For Part A, the average values coincide with the
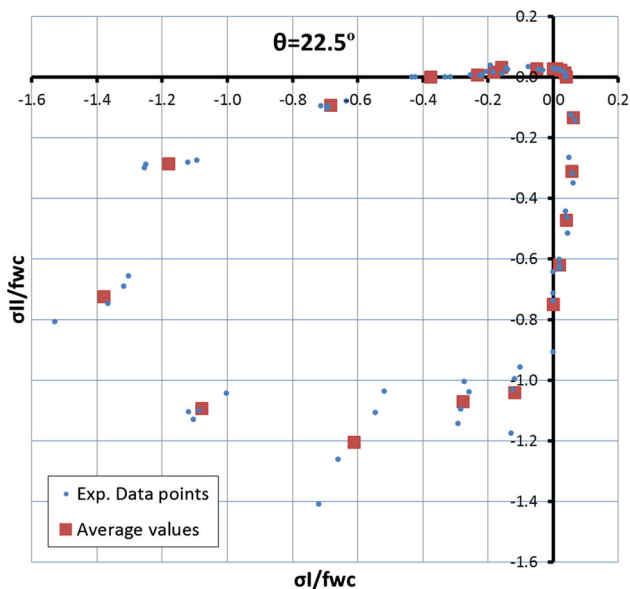
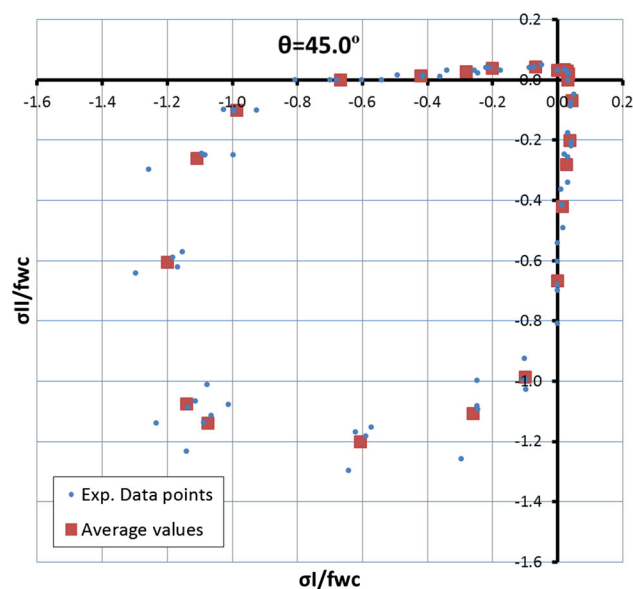**Fig. 5** Normalized experimental data and average values for the $\theta = 22.5°$ case

Fig. 6 Normalized experimental data and average values for the $\theta = 45.0°$ case

values themselves, as there is only one test performed for each σ_I/σ_{II} ratio.

For the data to be suitable for the neural network training, a conversion to polar coordinates (r, φ) is needed, where the distance (or radius, column 8) r is given by

$$r = \sqrt{\sigma_{I,aver}^2 + \sigma_{II,aver}^2} \qquad (1)$$

where $\sigma_{I,aver}$ and $\sigma_{II,aver}$ are the average stresses for each loading case (columns 5, 6).

Since we are trying to describe a full circle, the polar angle value φ has to be within $[0, 2\pi)$ range. Based on the values of σ_I and σ_{II}, we need to calculate the value of the polar angle φ. This can be done easily using the inverse tangent function (Arctan), which returns values within the $(-\pi, \pi)$ range, as follows:

$$\varphi_A = \text{Arctan}\left(\frac{\sigma_{II}}{\sigma_I}\right) \qquad (2)$$

$$\varphi_B = \varphi_C = \pi + \text{Arctan}\left(\frac{\sigma_{II}}{\sigma_I}\right) \qquad (3)$$

$$\varphi_D = 2\pi + \text{Arctan}\left(\frac{\sigma_{II}}{\sigma_I}\right) \qquad (4)$$

For cases where $\sigma_I = 0$, the above formulas do not apply and it is obviously $\varphi = \pi/2$ (for $\sigma_{II} > 0$) or $\varphi = 3\pi/2$ (for $\sigma_{II} < 0$). The angle φ is given in column 7 of the table. The figures below show the corresponding diagrams for the other four θ cases ($\theta = 22.5°$, $\theta = 45°$, $\theta = 67.5°$, $\theta = 90°$) (Figs. 5, 6, 7, 8).

It should be noted that the data for $\theta = 45°$ are symmetric with respect to the 45° diagonal line ($\sigma_I = \sigma_{II}$), due
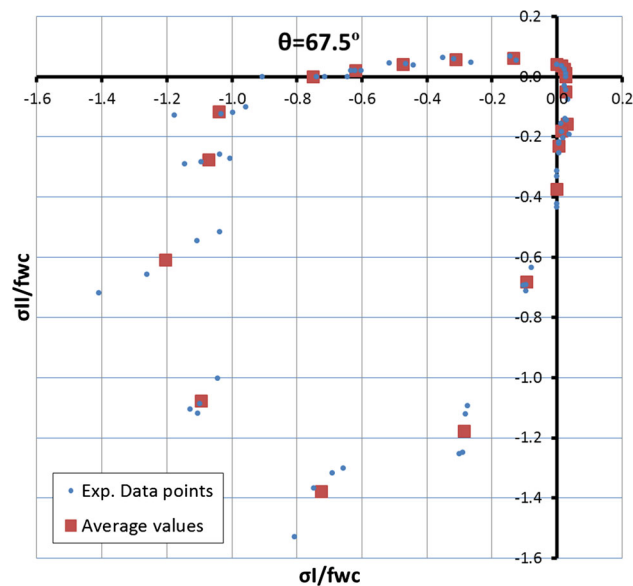
Fig. 7 Normalized experimental data and average values for the $\theta = 67.5°$ case

to not only the nature of the loading but also to the geometry of the masonry panel where for this special case (Fig. 3c) the bed joint orientation is equal to angle $\theta = 45°$. The data for $\theta = 0°$ and $\theta = 90°$ that correspond to complementary angles are also mutually symmetric to the line $\sigma_I = \sigma_{II}$. The same also applies for the data for $\theta = 22.5°$ and $\theta = 67.5$. These special conditions will be studied in detail in the next paragraphs.

For each of the five angles θ ($\theta = 0°$, 22.5°, 45°, 67.5°, 90°), a neural network is trained with the angle φ as its input
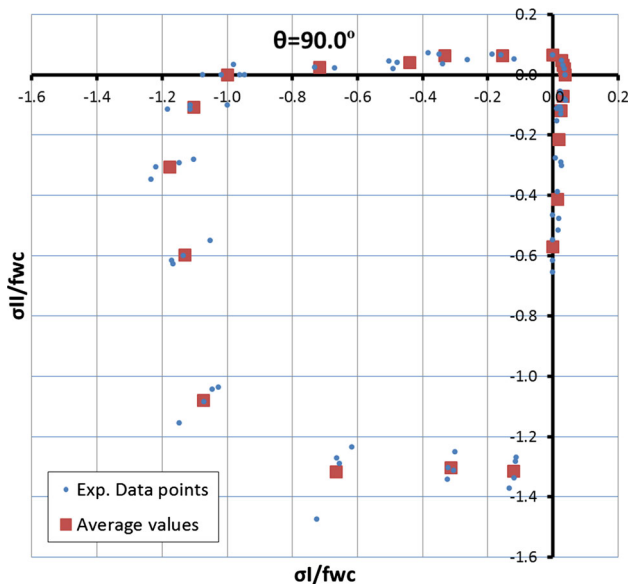
Fig. 8 Normalized experimental data and average values for the $\theta = 90.0°$ case

and the radius r as its output. Only the average values of each test (denoted as "square" points in the above figures) are used as training data for the neural networks. This proved to be the best strategy for handling this kind of problem, in order to avoid overtraining problems with the NN.

6.3 Properties of the curves: NN corrections

The failure curves have some distinct characteristics, and the NN results have to be in some cases corrected in order to follow the rules and comply with the characteristics. These characteristics are presented below.

6.3.1 Consistency for $\varphi = 0$ and $\varphi = 2\pi$

The case $\varphi = 0$ (start of circle) is in fact the same point as the case $\varphi = 2\pi$ (end of circle), and the results in these two points should coincide. Each curve has to be "closed," i.e. the two radius r_0 and $r_{2\pi}$ for $\varphi = 0$ and $\varphi = 2\pi$, respectively, have to be exactly the same. Also the tangents of the curve at $\varphi = 0$ and $\varphi = 2\pi$ have to coincide. The problem is depicted schematically in Fig. 9a.

For this reason, and in order to improve the performance of the NN, two measures have been taken:

1. Each NN is trained with two identical circles of data (instead of one circle which would normally be the case), so that the input corresponds to the angle φ in the range $[0, 4\pi]$ and as a result the data points are doubled. This measure helps the NN show a consistent behavior at $\varphi = 2\pi$ (end of circle). The number of data points for each case is given in Table 1.

2. The first measure mentioned above gives very good results, and it improved dramatically the performance of the NN. Although the problem is minimized, it still exists, in the sense that there is still a slight numerical difference between the NN-obtained r_0 and $r_{2\pi}$. In order to obtain a perfect, closed curve, a second measure is also taken. If r_0 is the predicted distance for the case $\varphi = 0$ and $r_{2\pi}$ is the predicted distance for the case $\varphi = 2\pi$, then we apply the following correction formulas:

$$\lambda = \frac{r_{2\pi}}{r_0} \tag{5}$$

Table 1 Number of data points for NN training, for each case

NN ID	Angle θ (°)	Number of NN data points
1	0	22 + 22 = 44
2	22.5	22 + 22 = 44
3	45	23 + 23 = 46
4	67.5	22 + 22 = 44
5	90	22 + 22 = 44
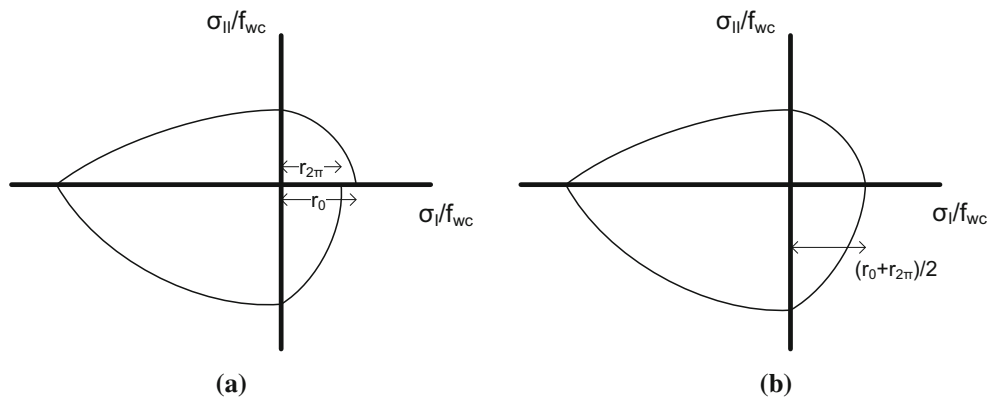
Fig. 9 Consistency for $\varphi = 0$ and $\varphi = 2\pi$. **a** Initial curve, **b** corrected curve
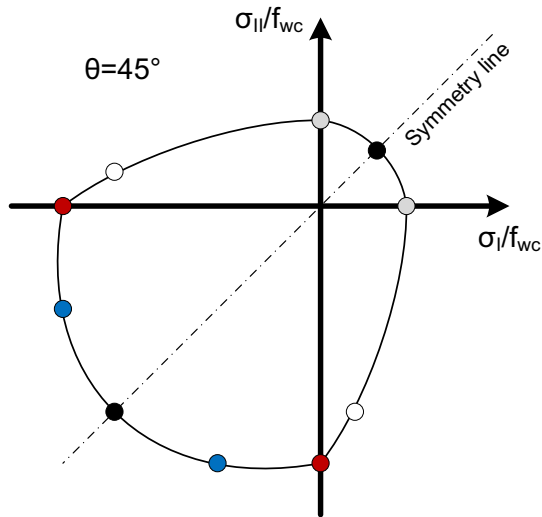
Fig. 10 Symmetry to the $\sigma_I = \sigma_{II}$ line, for the case $\theta = 45.0°$

Fig. 12 NN approximation result for $\theta = 0°$ (σ_{II} vs σ_I, dimensionless)
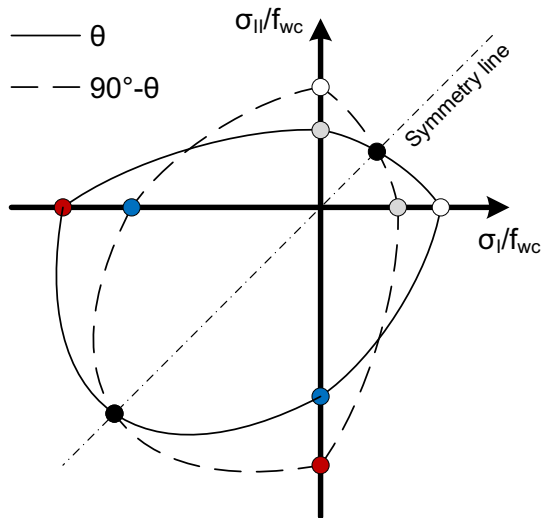
Fig. 11 Symmetry to the $\sigma_I = \sigma_{II}$ line, between curves corresponding to complementary angles (θ and $90° - \theta$)

$$k_1 = \frac{1 + \lambda}{2} \tag{6}$$

$$k_2 = \frac{1 + \lambda}{2\lambda} \tag{7}$$

$$r'_\varphi = r_\varphi \cdot \left[k_1 + \frac{\varphi}{2\pi} \cdot (k_2 - k_1) \right] \tag{8}$$

For $\varphi = 0$ or $\varphi = 2\pi$, Eq. (8) gives $(r_0 + r_{2\pi})/2$ which makes a closed curve, as shown in Fig. 9b. This correction is applied to the results of all NNs.

6.3.2 Symmetry for $\theta = 45°$

For the special case of masonry with bed joint angle $\theta = 45°$, the masonry panel exhibits a symmetry which
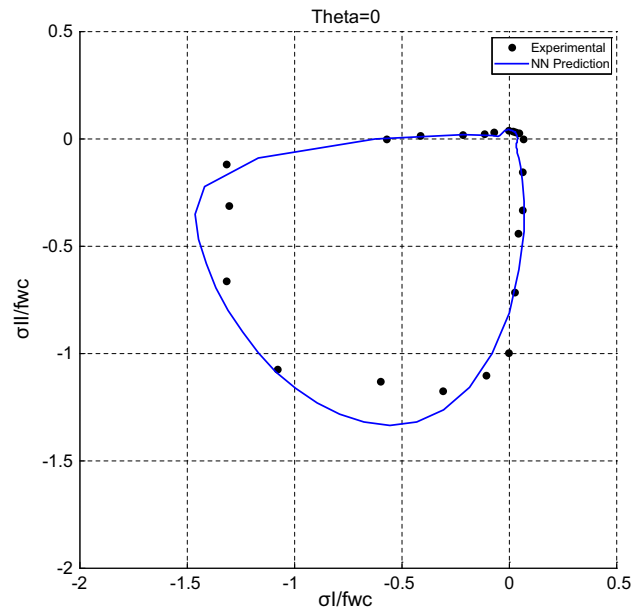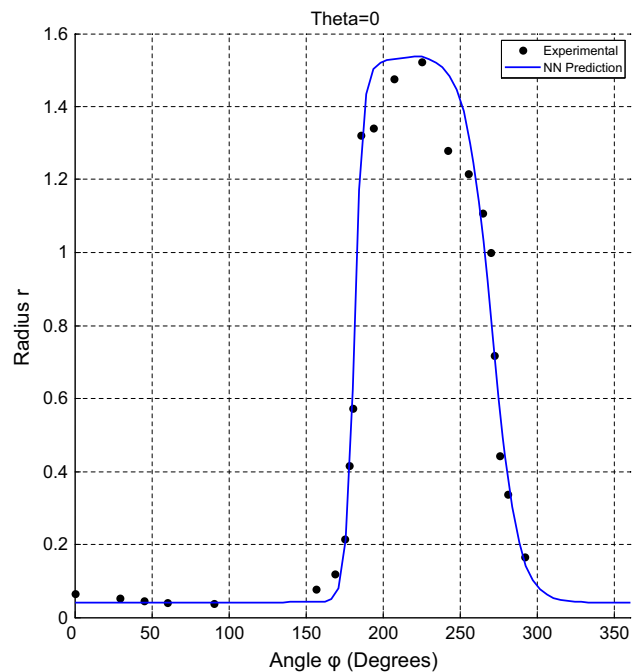
Fig. 13 NN approximation result for $\theta = 0°$ (Radius r vs Angle φ)

leads to a symmetric failure curve to the line $\sigma_I = \sigma_{II}$ as shown in Fig. 10.

Since the training data had already been symmetric, there were only slight differences in the NN results and the symmetry was only slightly disturbed. In any case, special care has been taken in order to obtain a perfectly symmetric result for this case. In particular, the results in the
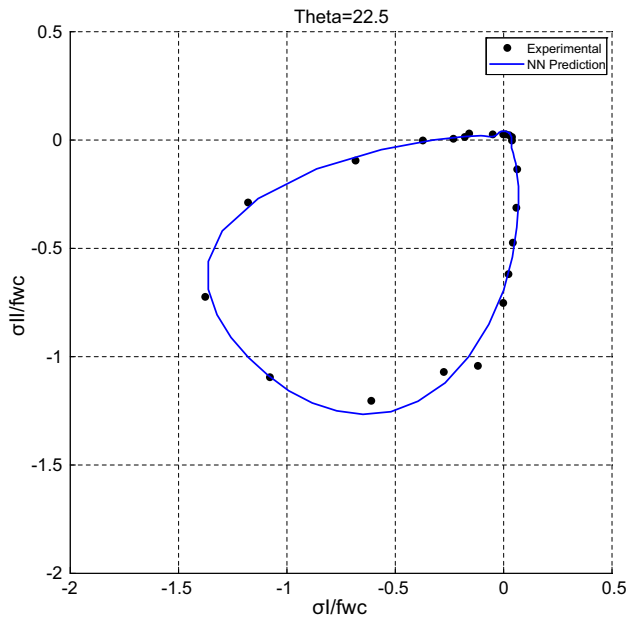
Fig. 14 NN approximation result for $\theta = 22.5°$ (σ_{II} vs σ_I, dimensionless)
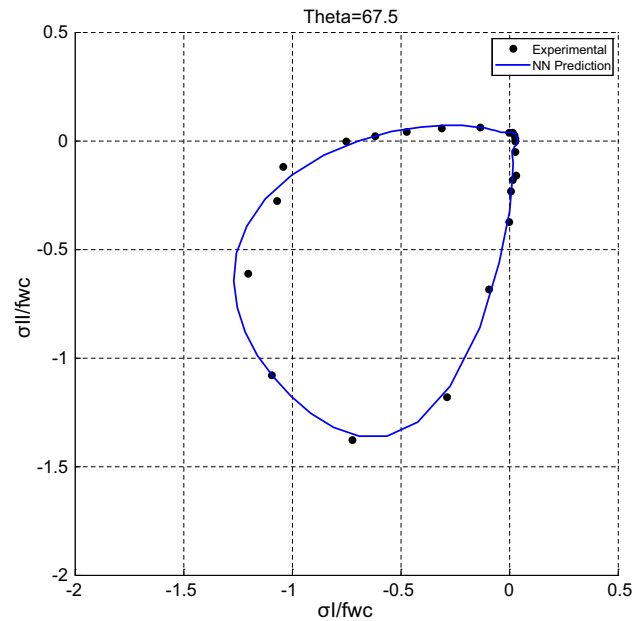
Fig. 16 NN approximation result for $\theta = 67.5°$ (σ_{II} vs σ_I, dimensionless)
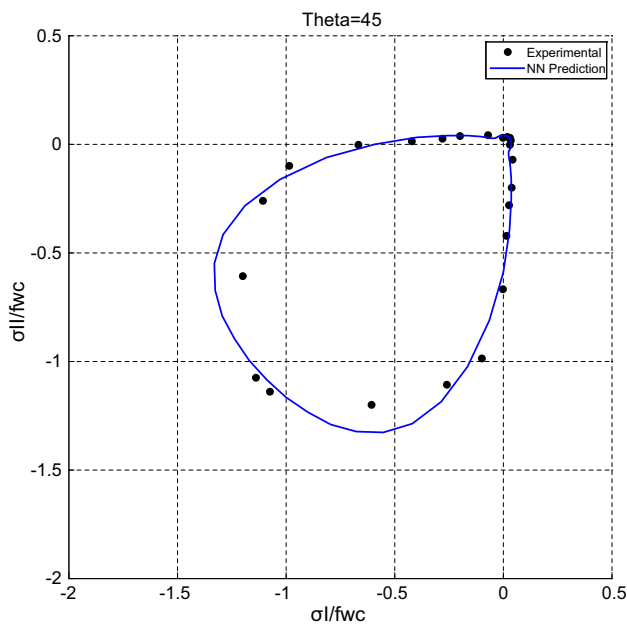
Fig. 15 NN approximation result for $\theta = 45°$ (σ_{II} vs σ_I, dimensionless)
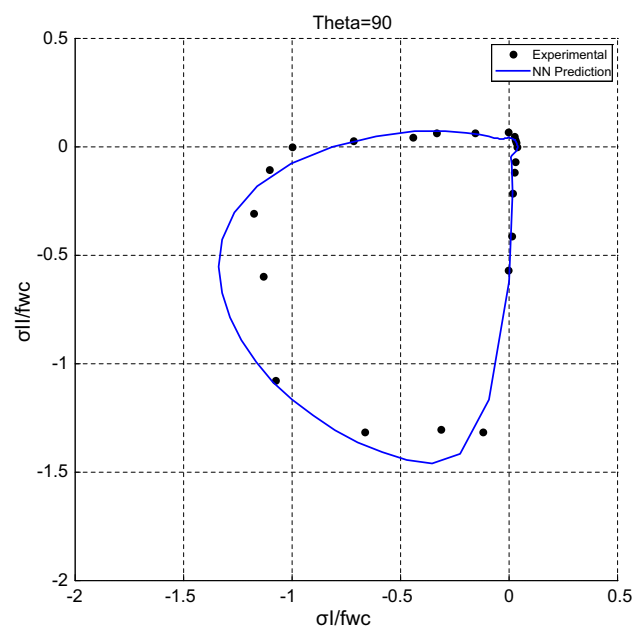
Fig. 17 NN approximation result for $\theta = 90°$ (σ_{II} vs σ_I, dimensionless)

two sides of the symmetry line were both taken into account and the average was finally considered, ensuring that the final result would be perfectly symmetric.

6.3.3 Symmetry for complementary angles (θ and $90° - \theta$)

It has been noted that the failure curves that correspond to complementary angles (θ and $90° - \theta$), such as $\theta = 0°$ and

$\theta = 90°$ as well as $\theta = 22.50°$ and $\theta = 67.5°$, are mutually symmetric to the line $\sigma_I = \sigma_{II}$ as shown in Fig. 11.

Although the results obtained by the NNs are satisfactory, we apply a special correction in order to ensure that the results for the case 0° are exactly equivalent to the results of the case 90° and also the results for the case 22.5° are equivalent to the results of the case 67.5°. In particular, the results of the two equivalent cases were both taken into
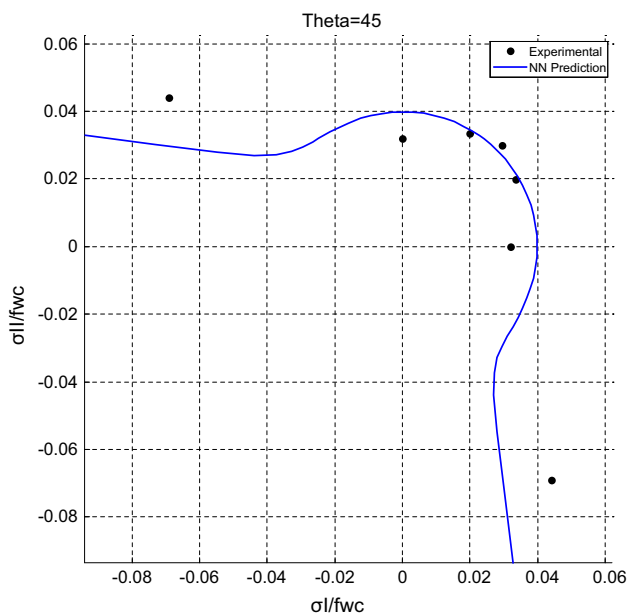
Fig. 18 NN approximation result for the case $\theta = 45°$, zoomed in

account and the average was finally considered, ensuring that the result would be perfectly symmetric between the two cases.

6.4 Final approximation results of the five NNs

The five NNs were trained with the input and output data of Tables 1, 2, 3, 4, 5 (last two columns) and then each NN was asked to produce the full curves for each bed joint angle, for a set of 80 segments (81 points). Although the NN was trained for two circles of data, it was asked to report results only for the first circle (in the range $[0, 2\pi]$). The results are shown in the figures below.

In all the figures (Figs. 12, 13, 14, 15, 16, 17, 18), the black dots denote the input data, i.e. the data corresponding to the last two columns of Tables 2, 3, 4, 5, 6. The blue curve denotes the NN prediction of the fitting curve. It can be seen that the NN managed to fit all the training data with very good accuracy, providing smooth curves in all cases.

Figure 15 shows the $\theta = 45°$ case, where it can be seen that the curve is perfectly symmetric to the $\sigma_I = \sigma_{II}$ line, because of the extra measures that have been taken. Figure 18 shows the same case ($\theta = 45°$), where we zoom in the tension–tension area. It is clear that the result is a perfectly closed curve. By comparing Fig. 12 ($\theta = 0°$) to Fig. 17 ($\theta = 90°$) and Fig. 14 ($\theta = 22.5°$) to Fig. 16 ($\theta = 67.5°$), it can be seen that the results for complementary angles are indeed symmetric to the $\sigma_I = \sigma_{II}$ line.

7 "Global" neural network model

In the previous part of the study, five NN Models were trained, each NN for one angle θ (0°, 22.5°, 45°, 67.5° and 90°). The final purpose of the study is to add also the angle θ as a parameter of the problem, thus creating a model that will be able to predict the entire failure curve not only for the predefined angles, but for any angle θ, from 0° to 90°.
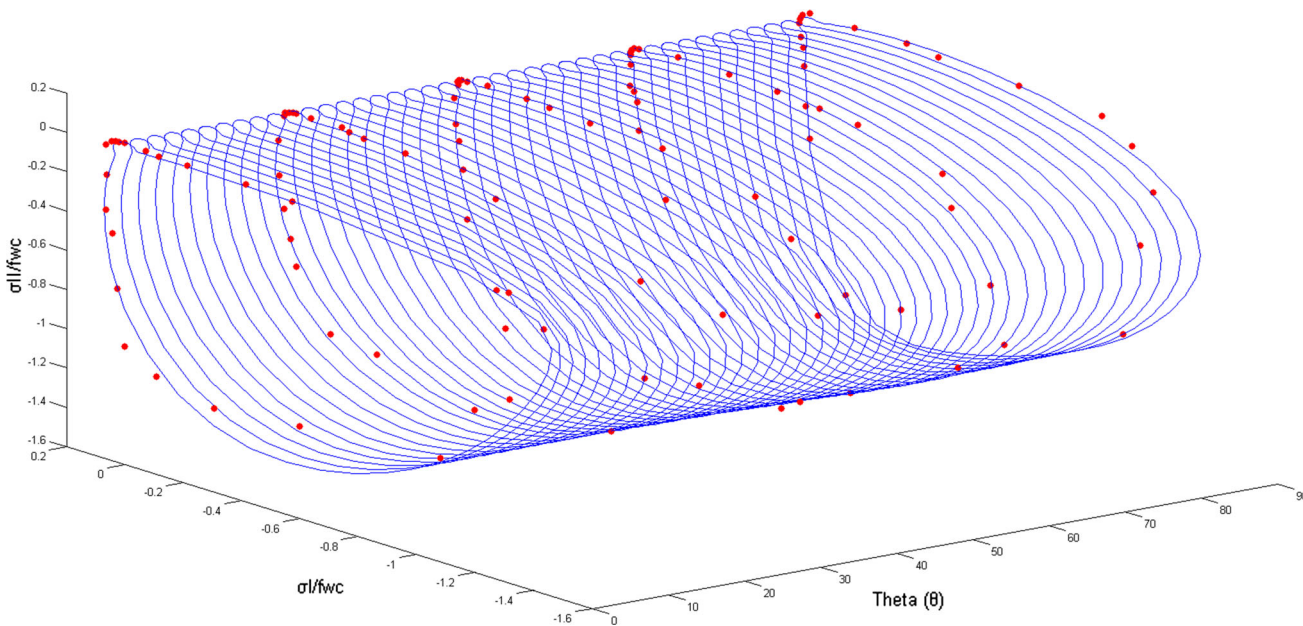
Fig. 19 Global NN approximation result of the 3D failure surface in terms of principal stresses (tube)
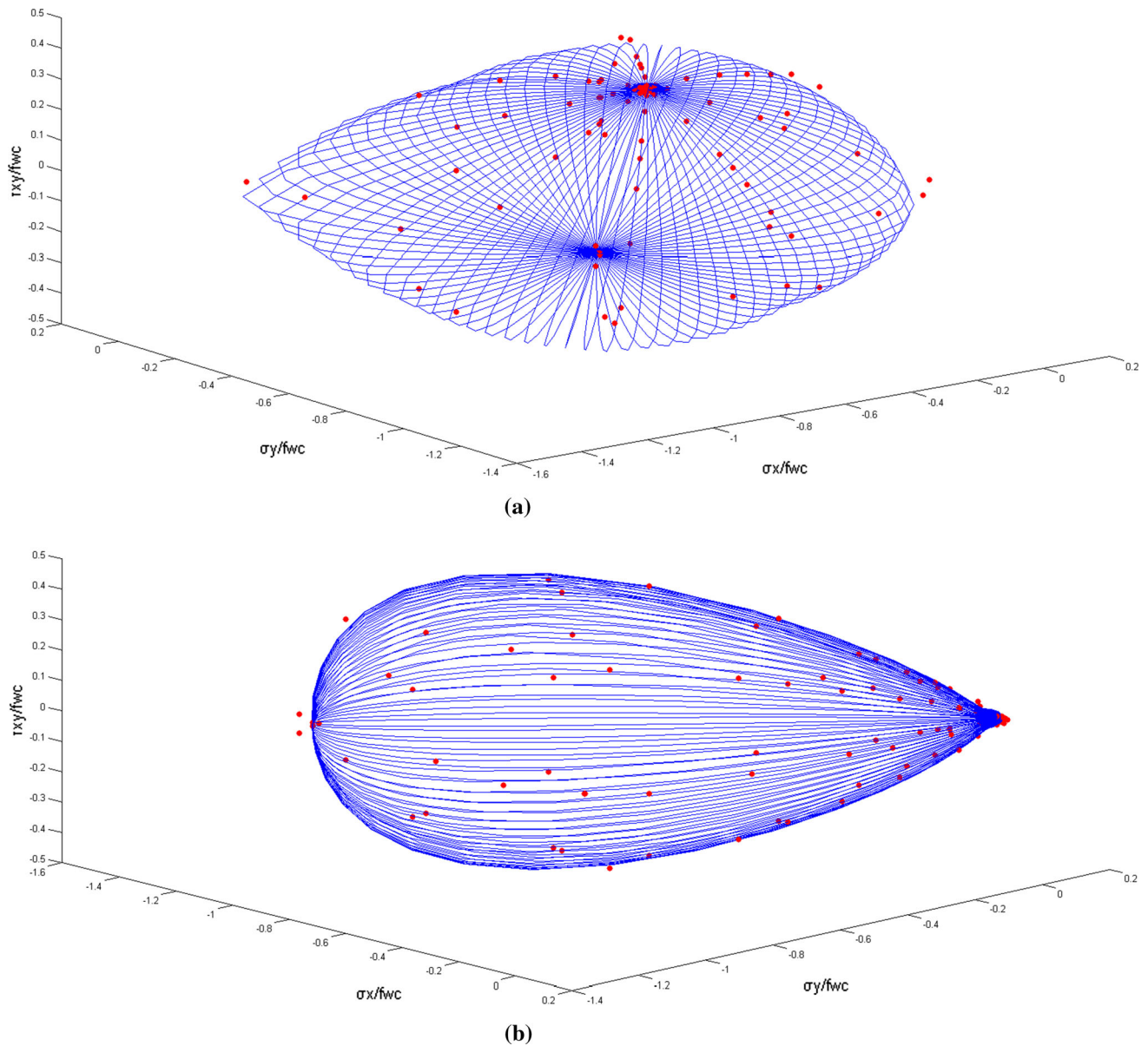
Fig. 20 Global NN approximation result of the 3D failure surface ("onion") in terms of normal stresses, two different views

In order to achieve this, after the five NNs were trained and they had provided their results, another bigger, "Global" NN was trained which took the results of the five NNs as inputs with the angle θ as an additional input, also. The new NN was then asked to fill also the gaps between the angles θ, providing the whole 3D failure "tube" for any angle θ and any angle φ (ratio of σ_{II}/σ_{I}), for all four quadrants.

The Global NN is also a BPNN with one hidden layer containing 10 nodes (2-10-1 architecture). The two inputs are the angles φ (0 to 4π—two full circles) and θ (0° to 90°), while the output is the distance (radius) r. The transfer function of the global NN is the hyperbolic tangent

function that was used also in the first five NNs. For the global NN, we use all the results of the other five NNs as training patterns. This means that we have $161*5 = 805$ training patterns, as we use 161 points $(80*2 + 1)$ for every angle θ (0°, 22.5°, 45°, 67.5° and 90°).

8 Global NN results

8.1 Failure tube in 3D

The global NN was trained and then it was asked to produce the whole 3D failure surface. Although the global NN

Fig. 21 The tensile area of the 3D failure "onion," zoomed in
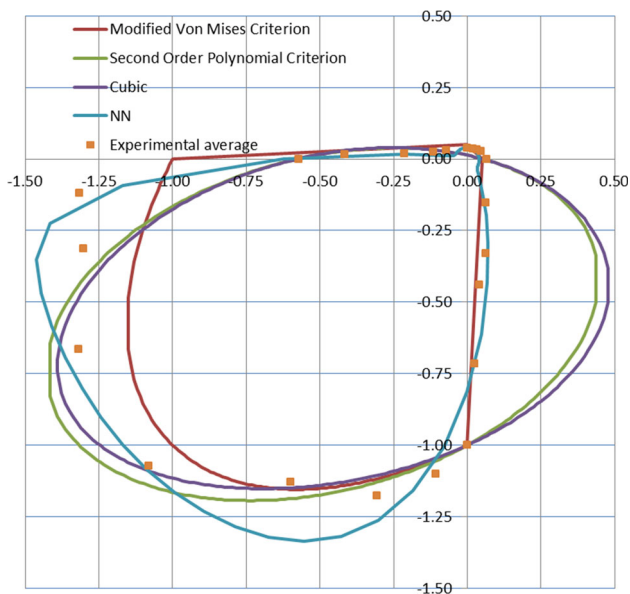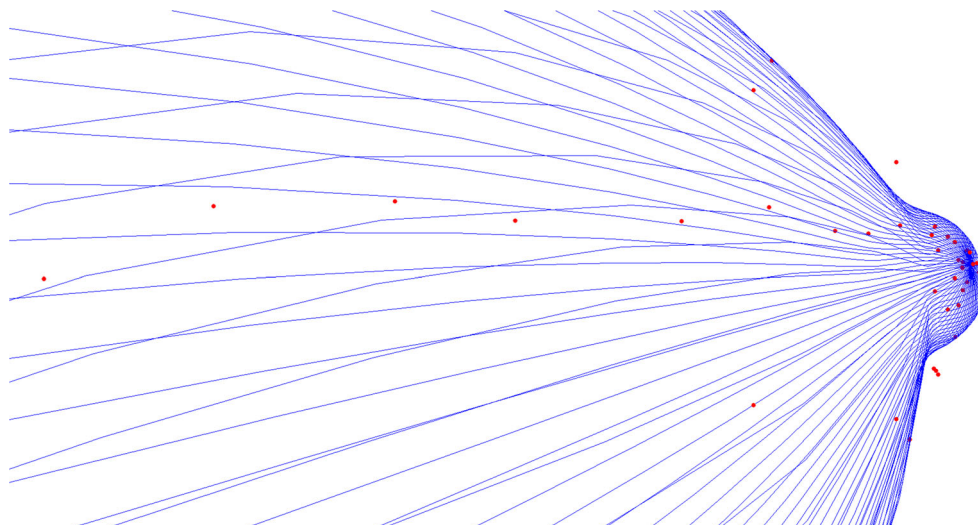
Fig. 22 Comparison of results for $\theta = 0.0°$
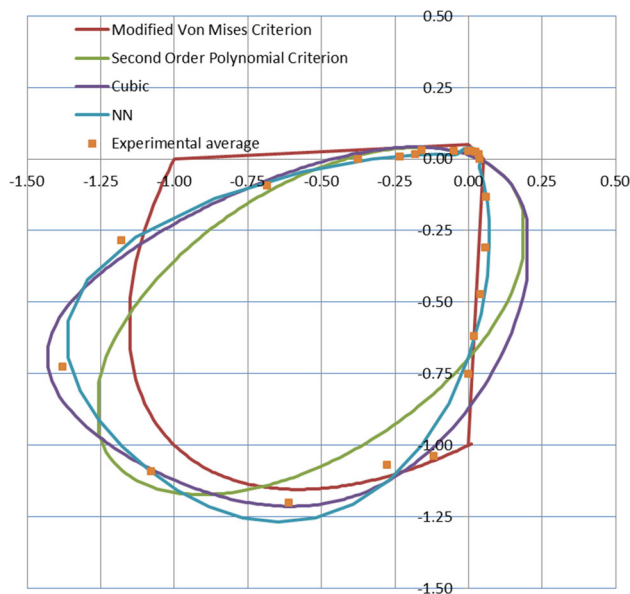
Fig. 23 Comparison of results for $\theta = 22.5°$

was trained in two full circles ($[0, 4\pi]$), in order to achieve better performance and to manage to "close" the curve for the first circle, it was asked to produce results only for the first circle ($[0, 2\pi]$). Specifically, the NN was asked to produce points where the angle φ was divided again in 160 (80*2) segments (161 points, each segment is equivalent to $360°/80 = 4.5°$), while angle θ is divided in 40 segments (41 points, each segment is equivalent to $90°/40 = 2.25°$). The figure below shows the result of the NN approximation in 3D. The red points (dots) denote the initial training set of the first five NNs, i.e. the average values gathered from the experimental results and used for the training of the initial NNs (Fig. 19).

8.2 Closed failure surface in 3D

Knowing the principal stresses σ_{I}, σ_{II} and the angle θ, we can obtain the corresponding values of σ_x, σ_y, $\tau_{xy} = \tau$, using the following well known formulas:

$$\sigma_x = \frac{1}{2}(\sigma_I + \sigma_{II}) + \frac{1}{2}(\sigma_I - \sigma_{II}) \cdot \cos(2\theta) \tag{9}$$

$$\sigma_y = \frac{1}{2}(\sigma_I + \sigma_{II}) - \frac{1}{2}(\sigma_I - \sigma_{II}) \cdot \cos(2\theta) \tag{10}$$

$$\tau = -\frac{1}{2}(\sigma_I - \sigma_{II}) \cdot \sin(2\theta) \tag{11}$$

This way we can convert the stresses from the system of the triplet $(\sigma_{\mathrm{I}}, \sigma_{\mathrm{II}}, \theta)$ to the one of the triplet $(\sigma_x, \sigma_y, \tau)$.
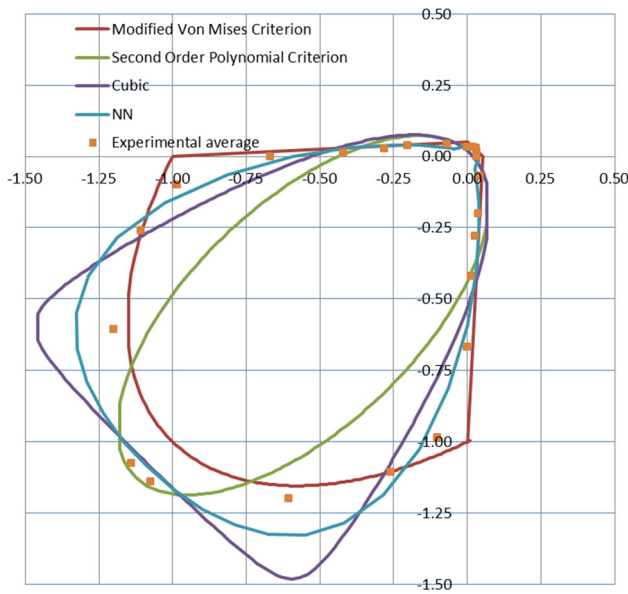
Fig. 24 Comparison of results for $\theta = 45.0°$
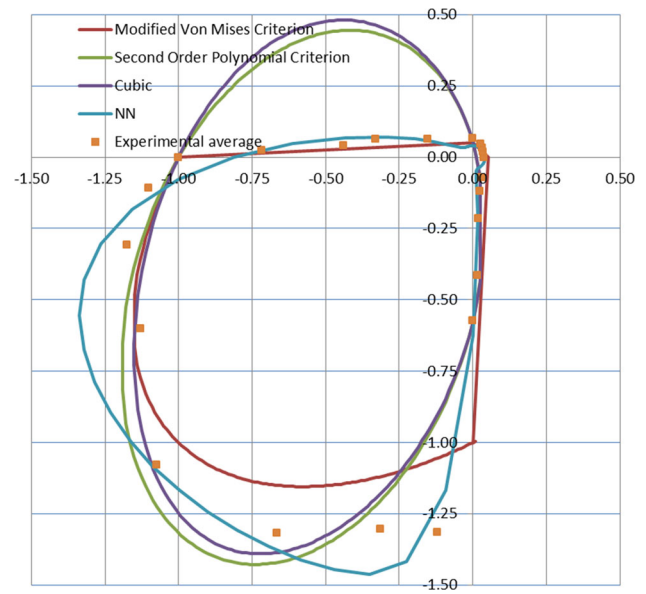
Fig. 26 Comparison of results for $\theta = 90.0°$

9 Comparison with other criteria: discussion

The results are compared to the main analytical criteria used to define the masonry failure surface [12]. To better facilitate the comparison, classical failure criteria have been used from the literature such as:

- The Von Mises modified failure criterion, which has been adopted by many researchers [46–50].
- The second-order polynomial, which comprises a simplified version of the cubic tensor polynomial, to be presented afterward. It applies to anisotropic materials and is commonly used to define the failure of masonry materials [26].
- The third-order polynomial or cubic tensor polynomial. This criterion comprises the generalization of the aforementioned failure criterion and has been applied to anisotropic composite materials [20, 51, 52] including masonry materials [24, 26].

All three failure criteria assume plane stress state and are expressed in terms of non-dimensionless normal stresses regarding the uniaxial compressive strength perpendicular to the bed joints of masonry $f_{wc}^{90°}$, as shown in [12]. Extensive and in-depth state-of-the-art reports on all the above criteria used for masonry can be found in [53, 54].

Figures 22, 23, 24, 25 and 26 show the comparison between the results obtained using the proposed NN methodology, in relation to the available analytical failure criteria, which were presented above, and the experimental

Fig. 25 Comparison of results for $\theta = 67.5°$

Figure 20 shows the failure curves in the 3D system of the triplet (σ_x, σ_y, τ), where an "onion" is formed. Again, the red points (dots) denote the initial training set of the first five NNs (primary training data).

Figure 21 shows the zoomed-in picture of the tensile area of the failure onion.

results obtained by Page [39–41]. Although some of the analytical failure criteria perform well in specific cases of the θ angle, and for specific quadrants of the stress state, it is often observed that in other cases they perform much worse, as they do not have the flexibility to adjust and give the whole picture for all angles and all quadrants. On the other hand, as shown in the figures, NN performs very well and shows the best overall (most balanced) performance compared to the other criteria.

10 Conclusions

Despite the plethora of analytical models that have been proposed for the modeling of masonry material, there is no analogous progress in models for the description of its failure surface, which is a prerequisite for a comprehensive and reliable implementation of them.

In the present study, an NN procedure for the modeling of the anisotropic masonry behavior under biaxial stress state is presented. In particular, a novel procedure based on neural network techniques has been introduced in order to model the failure/yield surface of masonry material in a dimensionless form. To this end, available classical

experimental results from the literature are used as input data for the training as well as the validation of NNs.

Being aware that masonry is a multi-phase material that exhibits distinct brittle and anisotropic nature with wide scatter in the values of its mechanical characteristics, the proposed NN procedure has been shown to be reliable and robust, providing valuable results.

In particular, the derived failure surface, on the one hand, fits the experimental data with high accuracy and on the other hand it is provided in a dimensionless form which is very important as it can be easily applied to other masonry materials of similar geometry and properties. Furthermore, the derived surface provides valuable information about areas of the masonry failure that have not been investigated until now (failure under heterosemous stresses or furthermore failure under biaxial tension for any tilt angle of the bed joints) helping us to better understand the whole fracture mechanics phenomenon.

Appendix

Tables 2, 3, 4, 5 and 6.

Table 2 Failure of brickwork under biaxial compression, $\theta = 0°$, and relevant calculations

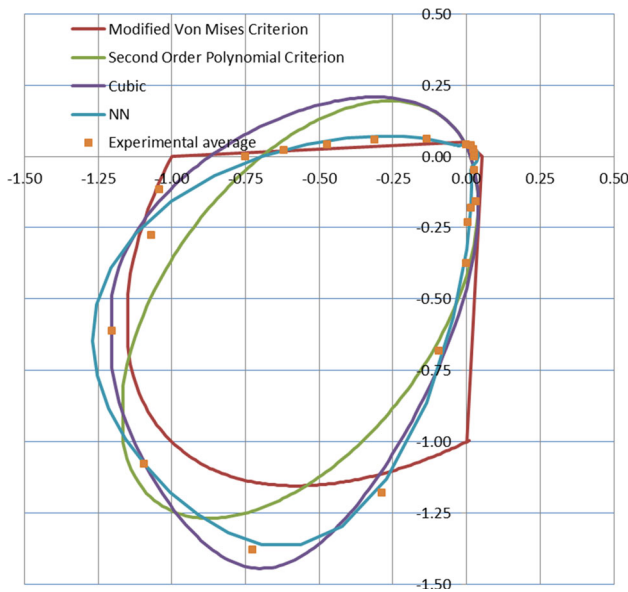| σ_I (MPa)	σ_{II} (MPa)	σ_I/f_{wc}	σ_{II}/f_{wc}	Average σ_I/f_{wc}	Average σ_{II}/f_{wc}	Angle φ	Radius r	Region, source
0.50	0.00	0.066	0.000	0.066	0.000	0.000	0.066	(A) Tension–tension
0.35	0.20	0.046	0.026	0.046	0.026	0.514	0.053	Page [39]
0.24	0.24	0.032	0.032	0.032	0.032	0.784	0.045	
0.15	0.26	0.020	0.035	0.020	0.035	1.050	0.040	
0.00	0.29	0.000	0.038	0.000	0.038	1.571	0.038	
−0.65	0.29	−0.086	0.039	−0.070	0.031	2.731	0.077	(B) Compression–tension
−0.61	0.26	−0.081	0.035					Page [41]
−0.45	0.19	−0.059	0.025					
−0.42	0.18	−0.056	0.024					
−0.99	0.19	−0.130	0.026	−0.115	0.023	2.947	0.118	
−0.89	0.18	−0.118	0.024					
−0.81	0.17	−0.107	0.023					
−0.81	0.14	−0.107	0.018					
−2.28	0.21	−0.302	0.028	−0.214	0.019	3.051	0.215	
−2.19	0.19	−0.290	0.025					
−1.16	0.09	−0.153	0.012					
−0.85	0.09	−0.112	0.012					
−3.90	0.13	−0.516	0.017	−0.414	0.015	3.106	0.415	
−3.60	0.14	−0.477	0.018					
−2.94	0.11	−0.388	0.015					
−2.09	0.07	−0.276	0.009					
−3.53	0.00	−0.467	0.000	−0.572	0.000	3.142	0.572	(C) Compression–compression
								Page [40]

Table 2 continued

σ_I (MPa)	σ_{II} (MPa)	σ_I/f_{wc}	σ_{II}/f_{wc}	Average σ_I/f_{wc}	Average σ_{II}/f_{wc}	Angle φ	Radius r	Region, source
−4.14	0.00	−0.548	0.000					
−4.66	0.00	−0.616	0.000					
−4.96	0.00	−0.656	0.000					
−9.59	−0.85	−1.269	−0.113	−1.316	−0.120	3.233	1.321	
−9.70	−0.87	−1.283	−0.115					
−10.11	−0.90	−1.338	−0.119					
−10.37	−1.01	−1.372	−0.133					
−9.46	−2.26	−1.252	−0.299	−1.303	−0.312	3.377	1.340	
−9.85	−2.43	−1.304	−0.322					
−9.92	−2.30	−1.312	−0.304					
−10.15	−2.45	−1.344	−0.324					
−9.33	−4.67	−1.235	−0.618	−1.318	−0.665	3.609	1.476	
−9.62	−5.01	−1.272	−0.663					
−9.74	−4.95	−1.289	−0.654					
−11.15	−5.48	−1.475	−0.724					
−7.84	−7.76	−1.037	−1.026	−1.080	−1.073	3.924	1.522	
−7.89	−7.91	−1.043	−1.046					
−8.20	−8.10	−1.085	−1.071					
−8.72	−8.67	−1.154	−1.147					
−4.16	−7.95	−0.550	−1.052	−0.599	−1.130	4.225	1.279	
−4.55	−8.57	−0.602	−1.134					
−4.66	−8.84	−0.616	−1.170					
−4.74	−8.81	−0.627	−1.165					
−2.12	−8.34	−0.281	−1.103	−0.307	−1.175	4.457	1.215	
−2.21	−8.67	−0.292	−1.147					
−2.32	−9.21	−0.306	−1.219					
−2.63	−9.32	−0.347	−1.233					
−0.76	−7.55	−0.100	−0.999	−0.107	−1.102	4.615	1.107	
−0.76	−8.42	−0.100	−1.114					
−0.87	−8.42	−0.115	−1.114					
−0.87	−8.93	−0.115	−1.182					
0.00	**−7.15**	0.000	−0.945	0.000	−1.000	4.712	1.000	
0.00	**−7.27**	0.000	−0.962					
0.00	**−7.69**	0.000	−1.018					
0.00	**−8.12**	0.000	−1.075					
0.15	−3.70	0.020	−0.490	0.025	−0.717	4.748	0.717	(D) Tension–compression
0.16	−5.06	0.021	−0.669					Page [41]
0.19	−5.52	0.025	−0.730					
0.26	−7.40	0.034	−0.979					
0.28	−2.55	0.037	−0.337	0.041	−0.440	4.806	0.442	
0.31	−3.62	0.041	−0.478					
0.34	−3.80	0.045	−0.503					
0.38	−1.99	0.050	−0.263	0.064	−0.331	4.904	0.337	
0.52	−2.63	0.069	−0.348					
0.55	−2.88	0.073	−0.382					
0.39	−0.90	0.052	−0.119	0.062	−0.154	5.097	0.166	
0.50	−1.19	0.066	−0.158					
0.52	−1.40	0.069	−0.185					

Table 3 Failure of brickwork under biaxial compression, $\theta = 22.5°$ and relevant calculations

σ_I (MPa)	σ_{II} (MPa)	σ_I/f_{wc}	σ_{II}/f_{wc}	Average σ_I/f_{wc}	Average σ_{II}/f_{wc}	Angle φ	Radius r	Region, source
0.30	0.00	0.040	0.000	0.040	0.000	0.000	0.040	(A) Tension–tension
0.28	0.11	0.037	0.015	0.037	0.015	0.378	0.040	Page [39]
0.18	0.18	0.024	0.024	0.024	0.024	0.777	0.034	
0.08	0.21	0.011	0.028	0.011	0.028	1.205	0.030	
0.00	0.21	0.000	0.028	0.000	0.028	1.571	0.028	
−0.56	0.26	−0.075	0.034	−0.050	0.028	2.636	0.057	(B) Compression–tension
−0.34	0.20	−0.045	0.026					Page [41]
−0.24	0.17	−0.031	0.023					
−1.45	0.29	−0.192	0.039	−0.158	0.031	2.947	0.161	
−1.08	0.22	−0.143	0.030					
−1.05	0.19	−0.139	0.025					
−1.54	0.14	−0.204	0.019	−0.182	0.015	3.057	0.182	
−1.39	0.11	−0.184	0.015					
−1.18	0.09	−0.157	0.012					
−1.92	0.05	−0.254	0.007	−0.231	0.006	3.115	0.232	
−1.68	0.04	−0.223	0.005					
−1.65	0.05	−0.218	0.006					
−2.37	0.00	−0.314	0.000	−0.375	0.000	3.142	0.375	(C) Compression–compression
−2.50	0.00	−0.331	0.000					Page [40]
−3.19	0.00	−0.422	0.000					
−3.28	0.00	−0.434	0.000					
−4.79	−0.60	−0.634	−0.079	−0.683	−0.093	3.277	0.689	
−5.24	−0.78	−0.694	−0.104					
−5.22	−0.71	−0.691	−0.094					
−5.38	−0.71	−0.712	−0.094					
−8.26	−2.08	−1.093	−0.275	−1.179	−0.286	3.380	1.213	
−8.47	−2.12	−1.120	−0.281					
−9.44	−2.18	−1.249	−0.289					
−9.47	−2.27	−1.253	−0.301					
−9.84	−4.96	−1.303	−0.657	−1.379	−0.725	3.626	1.558	
−9.95	−5.22	−1.317	−0.691					
−10.33	−5.65	−1.367	−0.748					
−11.56	−6.10	−1.530	−0.807					
−7.57	−7.89	−1.002	−1.044	−1.078	−1.094	3.934	1.536	
−8.22	−8.31	−1.087	−1.099					
−8.35	−8.53	−1.104	−1.128					
−8.46	−8.35	−1.119	−1.105					
−3.91	−7.83	−0.517	−1.036	−0.610	−1.204	4.243	1.349	
−4.12	−8.37	−0.545	−1.107					
−4.98	−9.54	−0.658	−1.262					
−5.43	−10.65	−0.719	−1.409					
−2.06	−7.59	−0.273	−1.005	−0.277	−1.070	4.459	1.105	
−1.95	−7.84	−0.259	−1.038					
−2.15	−8.27	−0.284	−1.094					
−2.20	−8.65	−0.291	−1.144					
−0.76	−7.23	−0.100	−0.956	−0.118	−1.040	4.600	1.047	
−0.89	−7.53	−0.118	−0.996					
−0.93	−7.80	−0.123	−1.032					

Table 3 continued

σ_I (MPa)	σ_{II} (MPa)	σ_I/f_{wc}	σ_{II}/f_{wc}	Average σ_I/f_{wc}	Average σ_{II}/f_{wc}	Angle φ	Radius r	Region, source
−0.98	−8.89	−0.129	−1.176					
0.00	−4.87	0.000	−0.644	0.000	−0.751	4.712	0.751	
0.00	−5.39	0.000	−0.713					
0.00	−5.59	0.000	−0.739					
0.00	−6.85	0.000	−0.907					
0.15	−4.55	0.020	−0.602	0.020	−0.619	4.745	0.620	(D) Tension–compression
0.15	−4.70	0.019	−0.622					Page [41]
0.16	−4.79	0.021	−0.634					
0.28	−3.34	0.038	−0.442	0.042	−0.474	4.800	0.475	
0.32	−3.51	0.042	−0.464					
0.34	−3.89	0.045	−0.515					
0.37	−2.00	0.048	−0.265	0.057	−0.311	4.893	0.316	
0.45	−2.40	0.059	−0.317					
0.47	−2.64	0.063	−0.350					
0.42	−0.95	0.055	−0.125	0.061	−0.134	5.142	0.148	
0.51	−1.08	0.068	−0.143					

Table 4 Failure of brickwork under biaxial compression, $\theta = 45°$ and relevant calculations

σ_I (MPa)	σ_{II} (MPa)	σ_I/f_{wc}	σ_{II}/f_{wc}	Average σ_I/f_{wc}	Average σ_{II}/f_{wc}	Angle φ	Radius r	Region, source
0.24	0.00	0.032	0.000	0.032	0.000	0.000	0.032	(A) Tension–tension
0.25	0.15	0.034	0.020	0.034	0.020	0.533	0.039	Page [39]
0.22	0.22	0.029	0.030	0.029	0.030	0.790	0.042	
0.15	0.25	0.020	0.034	0.020	0.034	1.038	0.039	
0.00	0.24	0.000	0.032	0.000	0.032	1.571	0.032	
−0.36	0.38	−0.048	0.050	−0.069	0.044	2.573	0.082	(B) Compression–tension
−0.55	0.32	−0.072	0.042					Page [41]
−0.65	0.30	−0.086	0.040					
−1.67	0.31	−0.220	0.042	−0.201	0.039	2.952	0.205	
−1.56	0.31	−0.207	0.042					
−1.33	0.24	−0.177	0.032					
−1.94	0.24	−0.257	0.032	−0.281	0.028	3.042	0.282	
−2.57	0.23	−0.340	0.031					
−1.86	0.16	−0.246	0.021					
−3.72	0.12	−0.492	0.016	−0.421	0.013	3.110	0.421	
−3.13	0.12	−0.414	0.015					
−3.14	0.09	−0.415	0.012					
−2.74	0.08	−0.362	0.011					
−4.09	0.00	−0.542	0.000	−0.667	0.000	3.142	0.667	(C) Compression–compression
−4.56	0.00	−0.603	0.000					Page [40]
−5.14	0.00	−0.681	0.000					
−5.29	0.00	−0.700	0.000					
−6.11	0.00	−0.808	0.000					
−6.99	−0.77	−0.925	−0.101	−0.985	−0.100	3.243	0.990	
−7.52	−0.72	−0.995	−0.095					
−7.52	−0.80	−0.995	−0.106					
−7.76	−0.74	−1.027	−0.098					

Table 4 continued

σ_I (MPa)	σ_{II} (MPa)	σ_I/f_{wc}	σ_{II}/f_{wc}	Average σ_I/f_{wc}	Average σ_{II}/f_{wc}	Angle φ	Radius r	Region, source
−7.54	−1.88	−0.997	−0.248	−1.108	−0.260	3.372	1.138	
−8.19	−1.88	−1.083	−0.248					
−8.27	−1.85	−1.094	−0.245					
−9.50	−2.24	−1.257	−0.297					
−8.71	−4.32	−1.153	−0.572	−1.200	−0.606	3.609	1.345	
−8.83	−4.70	−1.168	−0.621					
−8.94	−4.45	−1.183	−0.589					
−9.80	−4.86	−1.297	−0.643					
−8.14	−7.64	−1.077	−1.011	−1.140	−1.076	3.898	1.567	
−8.41	−8.05	−1.113	−1.065					
−8.59	−8.22	−1.136	−1.088					
−9.32	−8.61	−1.233	−1.139					
−7.64	−8.14	−1.011	−1.077	−1.076	−1.140	3.956	1.567	
−8.05	−8.41	−1.065	−1.113					
−8.22	−8.59	−1.088	−1.136					
−8.61	−9.32	−1.139	−1.233					
−4.32	−8.71	−0.572	−1.153	−0.606	−1.200	4.245	1.345	
−4.70	−8.83	−0.621	−1.168					
−4.45	−8.94	−0.589	−1.183					
−4.86	−9.80	−0.643	−1.297					
−1.88	−7.54	−0.248	−0.997	−0.260	−1.108	4.482	1.138	
−1.88	−8.19	−0.248	−1.083					
−1.85	−8.27	−0.245	−1.094					
−2.24	−9.50	−0.297	−1.257					
−0.77	−6.99	−0.101	−0.925	−0.100	−0.985	4.611	0.990	
−0.72	−7.52	−0.095	−0.995					
−0.80	−7.52	−0.106	−0.995					
−0.74	−7.76	−0.098	−1.027					
0.00	−4.09	0.000	−0.542	0.000	−0.667	4.712	0.667	
0.00	−4.56	0.000	−0.603					
0.00	−5.14	0.000	−0.681					
0.00	−5.29	0.000	−0.700					
0.00	−6.11	0.000	−0.808					
0.12	−3.72	0.016	−0.492	0.013	−0.421	4.744	0.421	(D) Tension–compression
0.12	−3.13	0.015	−0.414					Page [41]
0.09	−3.14	0.012	−0.415					
0.08	−2.74	0.011	−0.362					
0.24	−1.94	0.032	−0.257	0.028	−0.281	4.812	0.282	
0.23	−2.57	0.031	−0.340					
0.16	−1.86	0.021	−0.246					
0.31	−1.67	0.042	−0.220	0.039	−0.201	4.902	0.205	
0.31	−1.56	0.042	−0.207					
0.24	−1.33	0.032	−0.177					
0.38	−0.36	0.050	−0.048	0.044	−0.069	5.281	0.082	
0.32	−0.55	0.042	−0.072					
0.30	−0.65	0.040	−0.086					

Table 5 Failure of brickwork under biaxial compression, $\theta = 67.5°$ and relevant calculations

σ_I (MPa)	σ_II (MPa)	$\sigma_\mathrm{I}/f_\mathrm{wc}$	$\sigma_\mathrm{II}/f_\mathrm{wc}$	Average $\sigma_\mathrm{I}/f_\mathrm{wc}$	Average $\sigma_\mathrm{II}/f_\mathrm{wc}$	Angle φ	Radius r	Region, source
0.21	0.00	0.028	0.000	0.028	0.000	0.000	0.028	(A) Tension–tension
0.21	0.08	0.028	0.011	0.028	0.011	0.366	0.030	Page [39]
0.18	0.18	0.024	0.024	0.024	0.024	0.793	0.034	
0.11	0.28	0.015	0.037	0.015	0.037	1.193	0.040	
0.00	0.30	0.000	0.040	0.000	0.040	1.571	0.040	
−0.95	0.42	−0.125	0.055	−0.134	0.061	2.712	0.148	(B) Compression–tension
−1.08	0.51	−0.143	0.068					Page [41]
−2.00	0.37	−0.265	0.048	−0.311	0.057	2.961	0.316	
−2.40	0.45	−0.317	0.059					
−2.64	0.47	−0.350	0.063					
−3.34	0.28	−0.442	0.038	−0.474	0.042	3.054	0.475	
−3.51	0.32	−0.464	0.042					
−3.89	0.34	−0.515	0.045					
−4.55	0.15	−0.602	0.020	−0.619	0.020	3.109	0.620	
−4.70	0.15	−0.622	0.019					
−4.79	0.16	−0.634	0.021					
−4.87	0.00	−0.644	0.000	−0.751	0.000	3.142	0.751	(C) Compression–compression
−5.39	0.00	−0.713	0.000					Page [40]
−5.59	0.00	−0.739	0.000					
−6.85	0.00	−0.907	0.000					
−7.23	−0.76	−0.956	−0.100	−1.040	−0.118	3.254	1.047	
−7.53	−0.89	−0.996	−0.118					
−7.80	−0.93	−1.032	−0.123					
−8.89	−0.98	−1.176	−0.129					
−7.59	−2.06	−1.005	−0.273	−1.070	−0.277	3.395	1.105	
−7.84	−1.95	−1.038	−0.259					
−8.27	−2.15	−1.094	−0.284					
−8.65	−2.20	−1.144	−0.291					
−7.83	−3.91	−1.036	−0.517	−1.204	−0.610	3.611	1.349	
−8.37	−4.12	−1.107	−0.545					
−9.54	−4.98	−1.262	−0.658					
−10.65	−5.43	−1.409	−0.719					
−7.89	−7.57	−1.044	−1.002	−1.094	−1.078	3.920	1.536	
−8.31	−8.22	−1.099	−1.087					
−8.53	−8.35	−1.128	−1.104					
−8.35	−8.46	−1.105	−1.119					
−4.96	−9.84	−0.657	−1.303	−0.725	−1.379	4.228	1.558	
−5.22	−9.95	−0.691	−1.317					
−5.65	−10.33	−0.748	−1.367					
−6.10	−11.56	−0.807	−1.530					
−2.08	−8.26	−0.275	−1.093	−0.286	−1.179	4.474	1.213	
−2.12	−8.47	−0.281	−1.120					
−2.18	−9.44	−0.289	−1.249					
−2.27	−9.47	−0.301	−1.253					
−0.60	−4.79	−0.079	−0.634	−0.093	−0.683	4.577	0.689	
−0.78	−5.24	−0.104	−0.694					
−0.71	−5.22	−0.094	−0.691					
−0.71	−5.38	−0.094	−0.712					

Table 5 continued

σ_I (MPa)	σ_{II} (MPa)	σ_I/f_{wc}	σ_{II}/f_{wc}	Average σ_I/f_{wc}	Average σ_{II}/f_{wc}	Angle φ	Radius r	Region, source
0.00	−2.37	0.000	−0.314	0.000	−0.375	4.712	0.375	
0.00	−2.50	0.000	−0.331					
0.00	−3.19	0.000	−0.422					
0.00	−3.28	0.000	−0.434					
0.26	−0.56	0.034	−0.075	0.028	−0.050	5.218	0.057	(D) Tension–compression
0.20	−0.34	0.026	−0.045					Page [41]
0.17	−0.24	0.023	−0.031					
0.29	−1.45	0.039	−0.192	0.031	−0.158	4.907	0.161	
0.22	−1.08	0.030	−0.143					
0.19	−1.05	0.025	−0.139					
0.14	−1.54	0.019	−0.204	0.015	−0.182	4.797	0.182	
0.11	−1.39	0.015	−0.184					
0.09	−1.18	0.012	−0.157					
0.05	−1.92	0.007	−0.254	0.006	−0.231	4.739	0.232	
0.04	−1.68	0.005	−0.223					
0.05	−1.65	0.006	−0.218					

Table 6 Failure of brickwork under biaxial compression, $\theta = 90°$ and relevant calculations

σ_I (MPa)	σ_{II} (MPa)	σ_I/f_{wc}	σ_{II}/f_{wc}	Average σ_I/f_{wc}	Average σ_{II}/f_{wc}	Angle φ	Radius r	Region, source
0.29	0.00	0.038	0.000	0.038	0.000	0.000	0.038	(A) Tension–tension
0.26	0.15	0.035	0.020	0.035	0.020	0.520	0.040	Page [39]
0.24	0.24	0.032	0.032	0.032	0.032	0.787	0.045	
0.20	0.35	0.026	0.046	0.026	0.046	1.057	0.053	
0.00	0.50	0.000	0.066	0.000	0.066	1.571	0.066	
−0.90	0.39	−0.119	0.052	−0.154	0.062	2.757	0.166	(B) Compression–tension
−1.19	0.50	−0.158	0.066					Page [41]
−1.40	0.52	−0.185	0.069					
−2.88	0.55	−0.382	0.073	−0.331	0.064	2.950	0.337	
−2.63	0.52	−0.348	0.069					
−1.99	0.38	−0.263	0.050					
−2.55	0.28	−0.337	0.037	−0.440	0.041	3.048	0.442	
−3.62	0.31	−0.478	0.041					
−3.80	0.34	−0.503	0.045					
−3.70	0.15	−0.490	0.020	−0.717	0.025	3.106	0.717	
−5.06	0.16	−0.669	0.021					
−5.52	0.19	−0.730	0.025					
−7.40	0.26	−0.979	0.034					
−7.15	0.00	−0.945	0.000	−1.000	0.000	3.142	1.000	(C) Compression–compression
−7.27	0.00	−0.962	0.000					Page [40]
−7.69	0.00	−1.018	0.000					
−8.12	0.00	−1.075	0.000					
−7.55	−0.76	−0.999	−0.100	−1.102	−0.107	3.239	1.107	
−8.42	−0.76	−1.114	−0.100					
−8.42	−0.87	−1.114	−0.115					
−8.93	−0.87	−1.182	−0.115					
−8.34	−2.12	−1.103	−0.281	−1.175	−0.307	3.397	1.215	

Table 6 continued

σ_I (MPa)	σ_{II} (MPa)	σ_I/f_{wc}	σ_{II}/f_{wc}	Average σ_I/f_{wc}	Average σ_{II}/f_{wc}	Angle φ	Radius r	Region, source
−8.67	−2.21	−1.147	−0.292					
−9.21	−2.32	−1.219	−0.306					
−9.32	−2.63	−1.233	−0.347					
−7.95	−4.16	−1.052	−0.550	−1.130	−0.599	3.629	1.279	
−8.57	−4.55	−1.134	−0.602					
−8.84	−4.66	−1.170	−0.616					
−8.81	−4.74	−1.165	−0.627					
−7.76	−7.84	−1.026	−1.037	−1.073	−1.080	3.930	1.522	
−7.91	−7.89	−1.046	−1.043					
−8.10	−8.20	−1.071	−1.085					
−8.67	−8.72	−1.147	−1.154					
−4.67	−9.33	−0.618	−1.235	−0.665	−1.318	4.245	1.476	
−5.01	−9.62	−0.663	−1.272					
−4.95	−9.74	−0.654	−1.289					
−5.48	−11.15	−0.724	−1.475					
−2.26	−9.46	−0.299	−1.252	−0.312	−1.303	4.477	1.340	
−2.43	−9.85	−0.322	−1.304					
−2.30	−9.92	−0.304	−1.312					
−2.45	−10.15	−0.324	−1.344					
−0.85	−9.59	−0.113	−1.269	−0.120	−1.316	4.621	1.321	
−0.87	−9.70	−0.115	−1.283					
−0.90	−10.11	−0.119	−1.338					
−1.01	−10.37	−0.133	−1.372					
0.00	−3.53	0.000	−0.467	0.000	−0.572	4.712	0.572	
0.00	−4.14	0.000	−0.548					
0.00	−4.66	0.000	−0.616					
0.00	−4.96	0.000	−0.656					
0.07	−2.09	0.009	−0.276	0.015	−0.414	4.748	0.415	(D) Tension–compression
0.11	−2.94	0.015	−0.388					Page [41]
0.14	−3.60	0.018	−0.477					
0.13	−3.90	0.017	−0.516					
0.09	−0.85	0.012	−0.112	0.019	−0.214	4.803	0.215	
0.09	−1.16	0.012	−0.153					
0.19	−2.19	0.025	−0.290					
0.21	−2.28	0.028	−0.302					
0.14	−0.81	0.018	−0.107	0.024	−0.118	4.914	0.121	
0.17	−0.81	0.023	−0.107					
0.18	−0.89	0.024	−0.118					
0.19	−0.99	0.026	−0.130					
0.18	−0.42	0.024	−0.056	0.031	−0.070	5.123	0.077	
0.19	−0.45	0.025	−0.059					
0.26	−0.61	0.035	−0.081					
0.29	−0.65	0.039	−0.086					

References

1. Asteris PG, Chronopoulos MP, Chrysostomou CZ, Varum H, Plevris V, Kyriakides N, Silva V (2014) Seismic vulnerability assessment of historical masonry structural systems. Eng Struct 62–63:118–134

2. Caliò I, Marletta M, Pantò B (2012) A new discrete element model for the evaluation of the seismic behavior of unreinforced masonry buildings. Eng Struct 40:327–338

3. Lourenço PB, Rots JG, Blaauwendraad J (1998) Continuum model for masonry: parameter estimation and validation. J Struct Eng 124(6):642–652

4. Munjiza A (2004) The combined finite-discrete element method. Wiley, Chichester

5. Penna A, Lagomarsino S, Galasco A (2014) A nonlinear macroelement model for the seismic analysis of masonry buildings. Earthq Eng Struct Dyn 43(2):159–179

6. Reccia E, Milani G, Cecchi A, Tralli A (2014) Full 3D homogenization approach to investigate the behavior of masonry arch bridges: the Venice trans-lagoon railway bridge. Constr Build Mater 66:567–586

7. Lourenço PB (2002) Computations on historic masonry structures. Prog Struct Math Eng 4(3):301–319

8. Roca P, Cervera M, Gariup G, Pela L (2010) Structural analysis of masonry historical constructions. Classical and advanced approaches. Arch Comput Methods Eng 17(3):299–325

9. Asteris PG, Antoniou ST, Sophianopoulos DS, Chrysostomou CZ (2011) Mathematical macromodeling of infilled frames: state of the art. J Struct Eng 137(12):1508–1517

10. Asteris PG, Cotsovos DM, Chrysostomou CZ, Mohebkhah A, Al-Chaar GK (2013) Mathematical micromodeling of infilled frames: state of the art. Eng Struct 56:1905–1921

11. Sarhosis V (2012) Computational modelling of low bond strength masonry. PhD thesis, University of Leeds, UK

12. Plevris V, Asteris PG (2014) Modeling of masonry failure surface under biaxial compressive stress using neural networks. Constr Build Mater 55:447–461

13. Karantoni F, Fardis M, Vintzeleou E, Harisis A (1993) Effectiveness of seismic strengthening interventions. In: Proceedings of the IABSE symposium on the structural preservation of the architectural heritage, Roma, pp 549–556

14. Dhanasekar M, Page AW, Kleeman PW (1985) The failure of brick masonry under biaxial stresses. In: Proc. Inst. Civ. Eng., Part 2, vol 79, pp 295–313

15. Ganz HR (1989) Failure criteria for masonry. In: Proceedings if the of the 5th Canadian masonry symposium, pp 65–77

16. Ganz HR, Thurlimann B (1983) Strength of brick walls under normal force and shear. In: Proceedings of the 8th international symposium on load bearing brickwork, London, pp 27–29

17. Lourenço PB, De Borst R, Rots JG (1997) Plane stress softening plasticity model for orthotropic materials. Int J Numer Methods Eng 40:4033–4057

18. Massart TJ, Peerlings RHJ, Geers MGD, Gottcheiner S (2005) Mesoscopic modeling of failure in brick masonry accounting for three-dimensional effects. Eng Fract Mech 72(8):1238–1253

19. Pelà L, Cervera M, Roca P (2013) An orthotropic damage model for the analysis of masonry structures. Constr Build Mater 41:957–967

20. Tsai SW, Wu EM (1971) A general failure criterion for anisotropic materials. J Compos Mater 1971(5):58–80

21. Bland DR (1957) The associated flow rule of plasticity. J Mech Phys Solids 6:71–78

22. Koiter WT (1953) Sress-strain relations, uniqueness and variational theorems for elastic-plastic materials with singular yield surface. Q Appl Math 11:350–354

23. Zienkiewicz OC, Valliapan S, King IP (1969) Elasto-plastic solutions of engineering problems; initial stress finite element approach. Int J Numer Methods Eng 1:75–100

24. Asteris PG (2013) Unified yield surface for the nonlinear analysis of brittle anisotropic materials. Nonlinear Sci Lett A 4(2):46–56

25. Asteris PG (2010) A simple heuristic algorithm to determine the set of closed surfaces of the cubic tensor polynomial. Open Appl Math J 4:1–5

26. Syrmakezis CA, Asteris PG (2001) Masonry failure criterion under biaxial stress state. J Mater Civil Eng Am Soc Civil Eng (ASCE) 13(1):58–64

27. Adeli H (2001) Neural networks in civil engineering: 1989–2000. Comput Aided Civil Infrastruct Eng 16(2):126–142

28. Asteris PG, Tsaris AK, Cavaleri L et al (2016) Prediction of the fundamental period of infilled RC frame structures using artificial neural networks. Comput Intell Neurosci 2016:1–12. Art ID 5104907. doi:10.1155/2016/5104907

29. Lagaros ND, Plevris V, Papadrakakis M (2010) Neurocomputing strategies for solving reliability-robust design optimization problems. Eng Comput 27(7):819–840

30. Papadrakakis M, Lagaros ND, Plevris V (2004) Structural optimization considering the probabilistic system response. Theoret Appl Mech 31(3–4):361–394

31. Adeli H, Panakkat A (2009) A probabilistic neural network for earthquake magnitude prediction. Neural Netw 22(7):1018–1024

32. Panakkat A, Adeli H (2009) Recurrent neural network for approximate earthquake time and location prediction using multiple seismicity indicators. Comput Aided Civ Infrastruct Eng 24(4):280–292

33. Adeli H (1995) Knowledge engineering. Arch Comput Methods Eng 2(4):51–68

34. Ghaboussi J, Sidarta DE (1998) New nested adaptive neural networks (NANN) for constitutive modeling. Comput Geotech 22(1):29–52

35. Papadrakakis M, Lagaros ND, Tsompanakis Y (1998) Structural optimization using evolution strategies and neural networks. Comput Methods Appl Mech Eng 156(1–4):309–333

36. Papadrakakis M, Lagaros ND, Tsompanakis Y, Plevris V (2001) Large scale structural optimization: computational methods and optimization algorithms. Arch Computat Methods Eng 8(3):239–301

37. Singh R, Kainthola A, Singh TN (2012) Estimation of elastic constant of rocks using an ANFIS approach. Appl Soft Comput J 12(1):40–45

38. Unger JF, Eckardt S (2011) Multiscale modeling of concrete. Arch Comput Methods Eng 18(3):341–393

39. Page AW (1980) A biaxial failure criterion for brick masonry in the tension-tension range. Int J Mason Constr 1(1):26–29

40. Page AW (1981) The biaxial compressive strength of brick masonry. In: Proc. Inst. Civ. Eng., Part 2, vol 71, pp 893–906

41. Page AW (1983) The strength of brick masonry under biaxial tension-compression. Int J Mason Constr 3(1):26–31

42. Duan ZH, Kou SC, Poon CS (2013) Using artificial neural networks for predicting the elastic modulus of recycled aggregate concrete. Constr Build Mater 44:524–532

43. Naraine K, Sinha S (1991) Cyclic behavior of brick masonry under biaxial compression. J Struct Eng ASCE 117(5):1336–1355

44. Samarasinghe W (1980) The in-plane failure of brickwork. PhD thesis, University of Edinburgh

45. Tassios ThP, Vachliotis Ch (1989) Failure of masonry under heterosemous biaxial stresses. In: Proceedings of the international conference conservation of stone, masonry—diagnosis, repair and strengthening, Athens

46. El-Shafie A, Abdelazim T, Noureldin A (2010) Neural network modeling of time-dependent creep deformations in masonry structures. Neural Comput Appl 19(4):583–594

47. Bortolotti L, Carta S, Cireddu D (2005) Unified yield criterion for masonry and concrete in multiaxial stress states. J Mater Civ Eng 17(1):54–62

48. Dilrukshi KGS, Dias WPS (2008) Field survey and numerical modelling of cracking in masonry walls due to thermal movements of an overlying slab. J Natl Sci Found Sri Lanka 36(3):205–213

49. Hamid AA, Drysdale RG (1981) Proposed failure criteria for concrete block masonry under biaxial stresses. J Struct Div ASCE 107(ST8):1675–1687

50. Syrmakezis CA, Asteris PG, Sophocleous AA (1997) Earthquake resistant design of masonry tower structures. In: Proceedings, fifth international conference on structural studies of historical buildings, STREMA 97, 25–27 June, San Sebastian, Spain, pp 377–386

51. Jiang Z, Tennyson RC (1989) Closure of the cubic tensor polynomial failure surface. J Compos Mater 23(3):208–231

52. Wu EM (1972) Optimal experimental measurements of anisotropic failure tensors. J Comput Mater 6:472–480

53. Anthoine A (1992) In-plane behaviour of masonry: a literature review. Report EUR 13840 EN

54. Theodossopoulos D, Sinha B (2013) A review of analytical methods in the current design processes and assessment of performance of masonry structures. Constr Build Mater 41:990–1001